

Fabrication and Static Bending Properties of 3D Printed Zirconia Part via Digital Light Processing Method

Boran Wang

Beijing Institute of Technology <https://orcid.org/0000-0001-8683-4003>

Ali Arab

Beijing Institute of Technology

Jing Xie (✉ jxie@bit.edu.cn)

Beijing Institute of Technology <https://orcid.org/0000-0002-9376-2279>

Pengwan Chen

Beijing Institute of Technology

Research Article

Keywords: Zirconia, Digital Light Processing, Microstructure, Flexural Strength, Digital Image Correlation, Fractography

Posted Date: December 6th, 2021

DOI: <https://doi.org/10.21203/rs.3.rs-1130827/v1>

License:  This work is licensed under a Creative Commons Attribution 4.0 International License.

[Read Full License](#)

Fabrication and static bending properties of 3D printed zirconia part via digital light processing method

Boran Wang^a, Ali Arab^{b*}, Jing Xie^{a,b,c*} and Pengwan Chen^{a,b,c}

^a *State Key Laboratory of Explosion Science and Technology, Beijing Institute of Technology, 100081 Beijing, PR China.*

^b *Advanced Technology Research Institute, Beijing Institute of Technology, Jinan, 250307*

^c *Explosion Protection and Emergency Disposal Technology Engineering Research Center of the Ministry of Education, Beijing, 100081*

Corresponding author:

* Ali Arab, Email: arabali83@yahoo.com

* Jing Xie, Email: jxie@bit.edu.cn

Abstract

Zirconia is widely applied as an implant due to its' excellent biocompatibility and mechanical properties such as high hardness and extraordinary resistance to wear and corrosion. However, these outstanding mechanical properties make it challenging to fabricate Zirconia into complex shapes using conventional manufacturing techniques. In the current study, the digital light processing method was used to manufacture the Zirconia part. Its mechanical property was evaluated via a three-point bending test with digital image correlation and fractography analysis. The 3D-printed Zirconia sample had a relative density of approximately 98.8% and a Vickers hardness value of 1128 HV. The flexural strength under parallel and vertical bending loads (with respect to the printing direction) were $56.63\pm 3.97\text{MPa}$ and $70.98\pm 6.62\text{MPa}$, respectively. Surrounding by a few dense layers, the interior of the sintered sample was interlaced with needle-like and winding cracks. Under the three-point bending, the cracks initiated at the bottom surface due to the tension effect and propagated faster along the width direction than the thickness direction. There was a large area of cleavage morphology in the dense boundary layers, whereas the plastic fracture mode also appeared in the interior of the sintered samples. The digital light processing method is expected to be comparable to other advanced ceramic processing techniques for fabricating spatial lattice structural products.

Keywords: Zirconia; Digital Light Processing; Microstructure; Flexural Strength;
Digital Image Correlation; Fractography

1. Introduction

Ceramic materials are widely used in biomedical engineering, chemical industry and aerospace because of their excellent biocompatibility, wear resistance, heat resistance and corrosion resistance [1]. However, traditional manufacturing technology (gel casting, slip casting, dry pressing, injection molding, tape casting, and so on) is challenging to make ceramic materials into sophisticated shapes. As a result, it cannot take full advantage of their outstanding characteristics. In addition, there are particular issues in the conventional processes [2]: (1) The shaping process of complex parts highly depends on the mold; (2) Sintered bodies often need additional mechanical post-processing; (3) Certain unique shapes (e.g., inner cavities/pores/groove) are difficult to generate using traditional ways. Recently, it has been of great interest to use the Additive Manufacturing (AM, also known as 3D printing) [3] technique in the ceramic industry to sidestep the issues mentioned above and could save up 80% of the fabrication cost of the ceramic parts [4].

Usually, AM is classified according to the material state that is used (powder materials, solid materials, and liquid materials) [5] and the material accumulating (indirect, direct) [3]. However, the implementation of AM in the ceramic part fabrication has been much slower than in the polymer and metal parts fabrication due to the low surface quality and mechanical properties of ceramic parts fabricated by the available AM method compared to conventional methods [6–8]. Among the various AM techniques that be used for ceramic parts fabrication (three-dimensional printing (3DP) [9], stereolithography (SLA) [10], 3D gel-printing [11], a robocasting technique [12], direct inkjet printing (DIP) [13] and fused deposition modeling (FDM) [14], etc.), digital light processing (DLP) [4,15–23] is one of the

most promising technique. These parts fabricated by this technique exhibit fine surface finishing and very high spatial resolution. In this technique, a ceramic slurry is solidified layer by layer via UV-light exposure, and then the printed part is sintered to produce a fully dense sample.

Zirconia (ZrO_2) is a typical structural ceramic (known as the “ceramic steel” [24]) that is used as cutting tools and sensors. It is also used as an implant due to its excellent biocompatibility, mechanical properties, and satisfying aesthetics. Many researchers tried to use different AM techniques to fabricate the fully dense ZrO_2 part. He et al. [2] used the DLP technique to manufacture the complex dense ZrO_2 part. D. Komissarenko et al. [4] successfully printed Scandia-stabilized ZrO_2 parts by a DLP 3D printer, and no visible cracks or defects were observed in printed samples. They used 33 vol.% Scandia-stabilized ZrO_2 slurries for printing. This slurry is suitable to print the part by printing a thickness layer of 50 μm . Xia et al. [25] fabricated the fully dense ZrO_2 part by the direct ink writing technique. Yu et al. [26] used extrusion-based additive manufacturing to manufacture the ZrO_2 sample. The flexural strength of the samples fabricated by this method was much lower than the sample prepared conventionally. Recently, Sun et al. [27] studied the effect of the slurry and debinding process on the printing of the ZrO_2 .

The studies mentioned above mainly emphasize the preparation of slurry, the DLP printing parameters, the sintering process and the physic properties of the printed specimens, and only a limited investigation on the fractography analysis as well as the deformation mechanism. Therefore, the presented work prepared a high solid loading ZrO_2 slurry (55 wt.%) for DLP printing. The flexural strength of printed samples was measured via a three-point bending test

with the digital image correlation (DIC) method. Combining with the SEM and fractography analysis, the deformation mechanism was discussed before the conclusion section.

2. Methodology

2.1. Materials and slurry preparation

One of the critical steps in the DLP method is to prepare a photo-curable slurry with characteristics that meet the printing requirements (such as not having a high viscosity and appropriate curing characteristics). The following raw materials were used in this experiment: 3 mol% yttria-stabilized ZrO₂ (3Y-TZP), $D_{50} = 500\text{nm}$ (FREDS, JIANGSU FREDS POWDER TECHNOLOGY Co. Ltd, Yixing, China); 1,6-hexanediol diacrylate, HDDA, two shrink three propylene glycol acrylic ester, TPGDA, and the photoinitiator TPO (Diphenyl(2,4,6-trimethylbenzoyl) phosphine oxide, three of them from Yinchang Xin Cailiao Ltd, Shanghai, China). The dispersant was used DISPERBYK (a lower molecular weight polycarboxylic acid polymer (BYK Gardner GmbH, Geretsried, Germany)).

The process of powder modification and preparation of slurry is presented in Fig 1. The original ZrO₂ powder was humid, so it should be in an oven for drying thoroughly. After that, using 3 wt.% of DISPERBYK, based on the mass of ZrO₂ powder, was dissolved in ethanol solution by magnetic stirring at 60 °C. Then added a suitable amount of the dried ZrO₂ powder into the DISPERBYK solution grandly. Next, the resulting ZrO₂ slurry was magnetically stirred at water bath 60 °C for 1 h to promote the adsorption of the dispersant on the surface of the ZrO₂ particles adequately. Lastly, the modified ZrO₂ powder was dried at 70 °C for 24 h and then screened through a sieve.

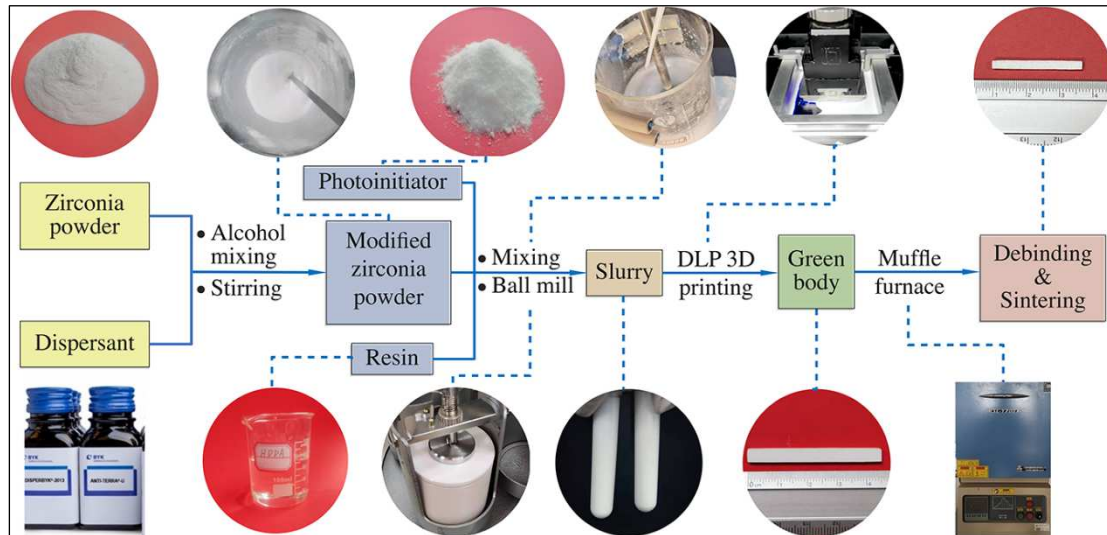


Fig. 1. The fabrication process of DLP 3D printing ZrO_2 .

First, HDDA (70g), TPGDA (33g) and TPO (1g) were mixed to obtain a homogeneous photosensitive resin. Next, the prepared photosensitive resin was added an appropriate amount (55 wt.%) of modified ZrO_2 powder, and stirred with a mixer for 15 minutes. Then the stable ZrO_2 slurry was achieved using a planetary ball mill for 4 hours (KE4, Ruiru Tec, Guangzhou, China) with a mass ratio of ZrO_2 grinding ball to ZrO_2 powder of 2:1.

2.2. DLP procedures

ZrO_2 samples were printed using a DLP 3D printer (Beijing TenDimensions Technology Co., Ltd. Beijing, China). First, the prepared ceramic slurry was poured into the scraper slot and spread slurry on the Teflon film. Then, UV light was exposed to the Teflon film surfaced, and the slurry was polymerized and cross-linked to form a single layer. After that, the Z - stage moved upwards, and the slurry was recoated on the Teflon film surface by scraper moving in the X-direction. Finally, this procedure was repeated to print the whole part. Fig. 2 schematically shows the DLP process.

The printed samples were cleaned by ultrasonic cleaning in deionized water with resin cleaner in order to remove the remaining slurry on the printed samples, and then dried at 60°C for 24 hours.

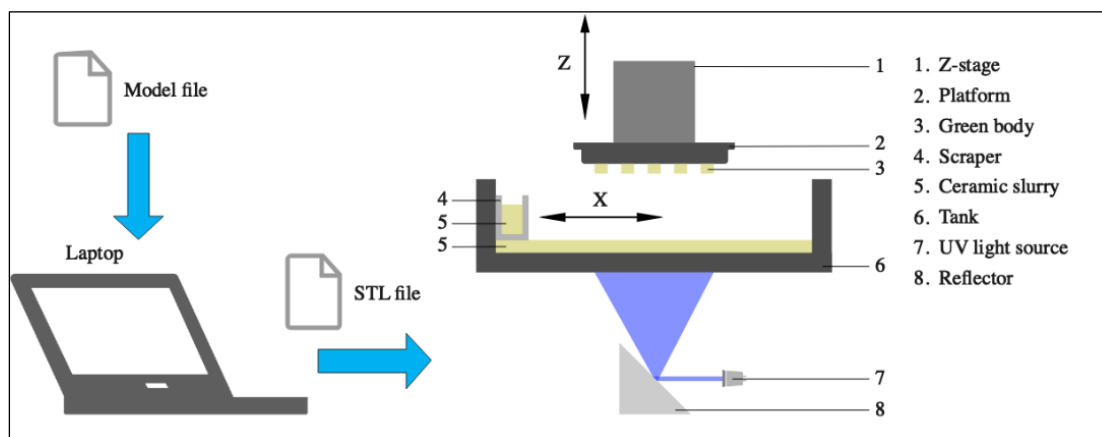


Fig. 2. The schematic diagrams of DLP 3D printing procedures.

2.3. *Debinding and sintering*

A one-step sintering method was adopted after trial and experiment since the samples became exceptionally fragile after debinding. The debinding and sintering process uses only a traditional muffle furnace (KSL-1700X, Hefei Kejing Material Technology Co., Ltd., China).

After printing the green parts, a debinding process must be performed to remove resin from the green body. The debinding process should be designed carefully to avoid the formation of cracks during it. The debinding behavior depends on several factors, such as resin composition, component geometry, and solid loading. For these reasons, the thermogravimetric analysis (TGA) and Derivative Thermogravimetry (DTG) of the cured slurry were performed and carried out on Thermo Gravimetric Analyzer type (METTLER TG/DSC3+, METTLER TOLEDO, USA).

Printed specimens must be sintered as fast as possible to avoid the potential effects of environmental conditions on the mechanical properties of the ceramics. The sintering process was described in detail in the results and discussion section.

2.4. Flexural strength tests

The dimensions of the specimens were 45 mm × 4 mm × 3 mm (length, width, thickness). Ceramics' mechanical behavior is largely dependent on the applied fabrication process, strain rate, and material type. According to ASTM C 1161-02c (2008), the three-point bending test (Fig.3) was carried out on a universal testing machine (ETM104B, WANCE, China). The three-point bending span was 20mm, and the loading rate was 0.3mm/min. Before testing, the samples were visually inspected to exclude artificial defects, the support structures were removed, and no further surface finishing was implemented after printing and cleaning. The mechanical test was terminated when the sample failed, and the maximum load obtained was used to calculate the flexural strength (σ_f).

$$\sigma_f = \frac{3PL}{2bd^2} \quad (1)$$

where P , L , b , and d are the maximum load (N), support span (mm), the width of the tested beam (mm), and the thickness of the tested beam (mm), respectively.

DIC technology was used to analyze the cracking process of the sintered ZrO₂ samples under the three-point bending test. The surface of the samples was photted at a speed of 3 frames per second by a CDD camera (GRAS-50S5M/C) with a pixel resolution of 5 million pixels. To obtain high-quality images measured by digital image correlation (DIC), two 95 W high-power LED lamps were used as light sources and provided adequate illumination intensity.

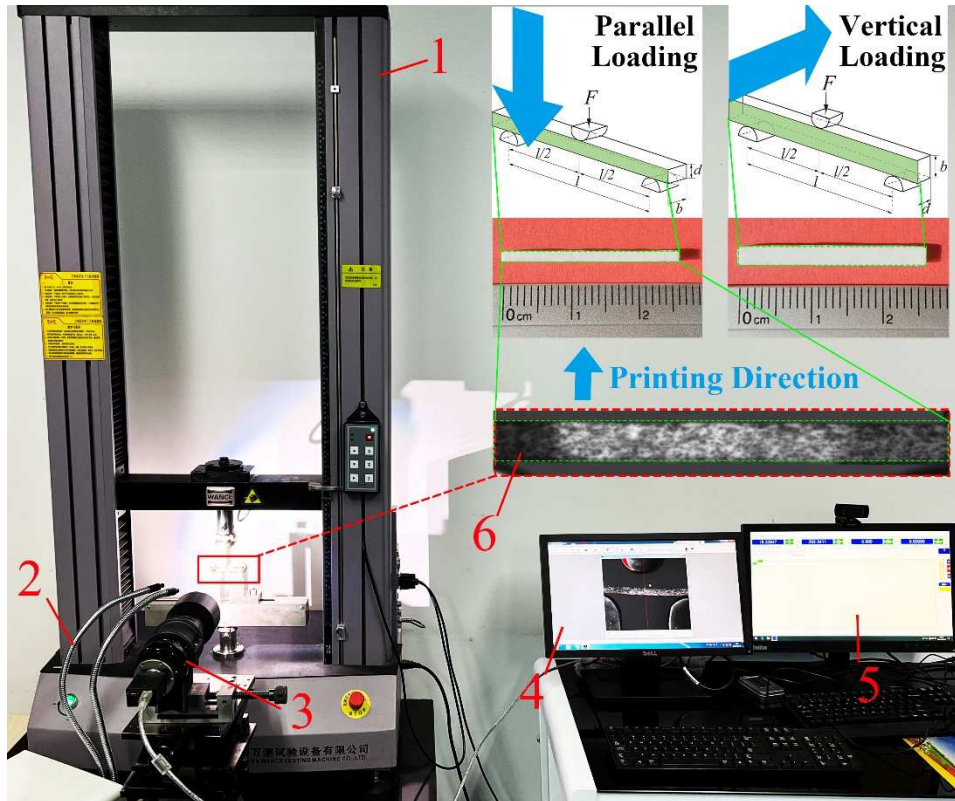


Fig. 3. Three-point bending test facility (1 - universal testing machine, 2 - light source, 3 - DIC camera, 4 - DIC camera data acquisition, 5 - testing machine data acquisition, 6 - specimen).

2.5. Characterization

A rheometer (Physica MCR301, Anton Paar, Austria) was used to study the rheological behavior of the ceramic slurry. The functional relationship between viscosity and shear rate was measured in the range of $0\text{--}200\text{ s}^{-1}$ under isothermal conditions ($25.0\text{ }^{\circ}\text{C}$).

The shrinkage of sintered samples was measured via a Vernier caliper. The apparent density and open porosity of the sintered sample were determined by True Density Analyzer (AccuPyc II 1345, Micromeritics instrument Ltd. U.S.A). Vickers hardness was determined using the Vickers indentation method at an indentation load of 9.8 N for 15 seconds (HMV-2TADW, Shimadzu Corporation, Japan). For phase identification, an X-ray diffractometer (XRD) (Bruker AXSD2 Advance, Billerica, MA, USA) was utilized. The microstructures and

the fracture surfaces of samples were examined using the scanning electron microscope (SEM) (SU100, HITACHI, Japan).

3. Results and Discussion

3.1. Rheological properties

The slurry used in the DLP printing process should have high fluidity to ensure the printing of ceramic parts with complex geometry within a reasonable processing time, meaning the slurry viscosity should not be too high. The viscosity of 3 Pa·s at a shear rate of 10s^{-1} is generally considered to be the upper limit of processable slurry [28]. The rheology of slurry is affected by the dispersant property. Sun et al. [29] prepared the slurry with five various dispersants (oleic acid, coupling agent KH560, stearic acid, Disperbyk, and variquat CC42 NS). It was found that 3 wt.% Disperbyk is the best option, that's why the same type and amount of dispersant was used in this research. Fig.4 shows the rheological properties of the ZrO_2 slurry. The viscosity at 10 s^{-1} and 100 s^{-1} are $0.9\text{ Pa}\cdot\text{s}$ and $0.13\text{ Pa}\cdot\text{s}$, respectively. The prepared slurry revealed shear-thinning fluid behavior, indicating the slurry was appropriate for printing processing.

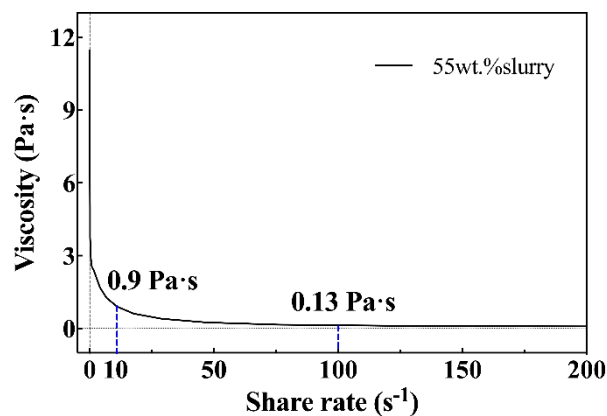


Fig. 4. Shear viscosity (η) of ZrO₂ slurry with respect to the shear rate in the range of [0, 200] (s⁻¹).

3.2. Sintering profile

Fig. 5(a) illustrates the TG-DTG curves of the green body obtained after DLP printing. The cured resin began to decompose at 80 °C, and finished at 540 °C. There were four prominent decomposition peaks around 180 °C, 360 °C, 410 °C, and 480 °C. The resin decomposed quickly between 180 °C and 410 °C during the debinding process.

Fig. 5(b) shows the temperature scheme used in the debinding and sintering. In the debinding sintering process, the pores among the powders were squeezed and eliminated, and a highly dense component was formed. In the low-temperature stage, the rapid expansion of gas would accelerate the initiation and growth of cracks [30]. Thus, the heating rate between 80 °C and 540 °C should be delicately controlled: various heating rates of 1 °C / min and 0.2 °C / min were implemented for the temperature range of RT - 80 °C and 80 - 540 °C. Meanwhile, in order to assure the fully chemical decomposition, one-hour dwelling time was applied at temperatures of 180 °C, 360 °C, 410 °C, 480 °C, and 540 °C, respectively. Moreover, a heating rate of 5 °C/min was selected for the entire sintering process up to 1500 °C, and kept for another 200 mins.

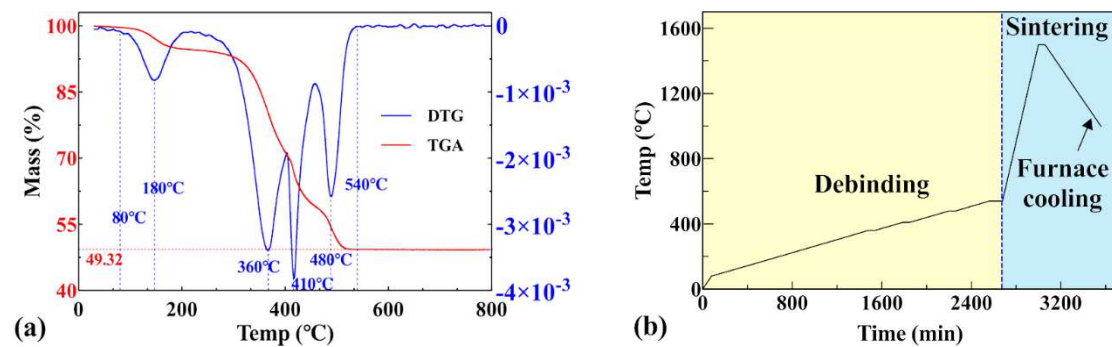


Fig. 5. (a) The TG/DTG curves and (b) the debinding and sintering profiles of the green body.

3.3. Physical properties of the printed sample

In DLP printing, curing thickness is a significant parameter determining the thickness of available layers and printing quality. Therefore, appropriate exposure times and light intensity must be found to ensure good bonding between cured layers during printing. After the preliminary test, the exposure time was determined as 2 s with a light intensity of 18 mW/cm², and the average curing thickness was measured as 35 μ m.

The insets in Fig. 3 show the sintered sample's front surface (along the printing direction) and the top surface (perpendicular to the printing direction). Good flatness can be observed on the top surface, and this uniform pattern shows the precision of the printing process.

The density of the sintered ZrO₂ sample was around 5.98 g/cm³, which was approximately 98.8% relative density (the theoretical density was taken as 6.05 g/cm³). This relative density was slightly lower than that of other samples (99%) prepared by the DLP method [31], which resulted in lower Vickers hardness values (1128 HV) of the sample compared to the sample with higher relative density (~1190 HV) [31].

The variation of the anisotropic linear shrinkage of the sintered specimen is listed in Table 1. Due to the friction between the specimen and crucible during sintering, the linear shrinkage in the width (*b*) direction was slightly lower than that in the thickness (*d*) direction. Reducing cracks and improving repeatability and dimensional precision was profit from lower linear shrinkage and shrinkage deviation.

Table 1
Shrinkages of the samples.

Direction (n = 13)	Shrinkage (%)	Mean+SD.	Mean+SEM.
Thickness, <i>d</i>	41.90	0.7659	0.2124
Width, <i>b</i>	41.58	0.8199	0.2274
Average	41.74	0.4991	0.1384

*SD.: Standard Deviation *SEM.: Standard Error of Mean

3.4. XRD

Cubic ZrO_2 (c- ZrO_2) exists at temperatures higher than 2370°C . Tetragonal ZrO_2 (t- ZrO_2) exists between 1170 and 2370°C . When the temperatures are lower than 1170°C , the phase transition from t- ZrO_2 to monoclinic ZrO_2 (m- ZrO_2) occurs [32]. The phase of t- ZrO_2 , however, can be retained at RT by adding metal oxides, such as yttria (Y_2O_3). The crystalline phase of m- ZrO_2 and t- ZrO_2 were both detected in the original ZrO_2 powder because the 3 mol% Y_2O_3 -stabilized ZrO_2 powder was used in the present study (Fig. 6). However, after sintering up to 1500°C , the amount of m- ZrO_2 was below the detection limit in the specimen due to the m \rightarrow t phase transition. As a result, the prominent peaks of 2θ at 30.2° , 34.7° , and 35.2° became more significant (Fig. 6). These three peaks corresponded to the characteristic crystal planes (101)t, (002)t, and (110)t of t- ZrO_2 , respectively.

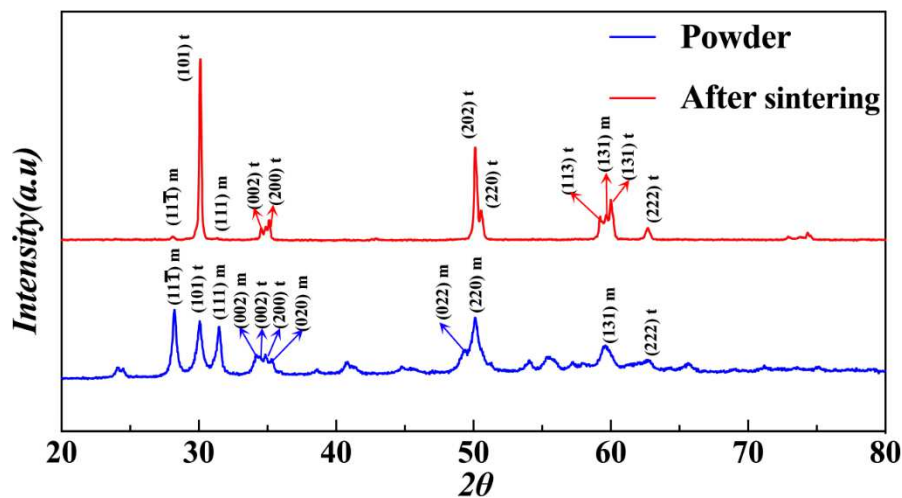


Fig. 6. The XRD pattern of the original ZrO_2 powder and the sintered ZrO_2 sample.

3.5. Mechanical property

The force-displacement curves of the samples under parallel and vertical bending loads (with respect to the printing direction) are shown in Fig. 7. The flexural strength under parallel and vertical bending loads were $56.63\pm 3.97\text{MPa}$ and $70.98\pm 6.62\text{MPa}$, respectively.

There is still a certain gap between the results in this study and better levels achieved in other literature [16]. But this lower strength may be able to provide better biocompatibility by avoiding the stress shielding phenomenon. The values of elastic modulus and strength of cancellous bone are 10 to 1570 MPa and 1.5 to 38 MPa, respectively [33]. The researchers have been designed and successfully printed various ceramic bone scaffold [15,21,23]. The DLP-printed ZrO_2 with different lattice structures would show great potential in the implant field.

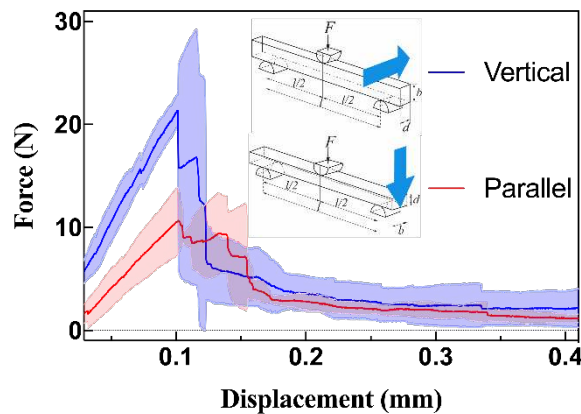


Fig. 7. The flexural strength curves.

The measured horizontal (e_{xx}) and vertical strain (e_{yy}) on the surface of the specimen are given in Fig. 8 for the parallel loading and Fig. 9 for the vertical loading. The crack initiated at the sample bottom surface due to the tension effect and developed upward until the failure of the samples. The material under tension during testing influenced the flexural strength and the failure mode of the experimental groups [34]. Clearly, the crack propagated through the width direction (under vertical loading) was

faster than that propagated through the thickness direction (under parallel loading). One of the key reasons that affect the flexural strength of the specimen is the existence of cavities in the specimen. During the three-point bending test, if a cavity is present at any point, the specimen tends to break quicker than the solid portion, and the strength decreases. A detailed fractography analysis will be given in the next section, combined with the SEM images.

Surface treatment has an important influence on flexural strength. The flexural strength of ceramics can be improved by some surface modification methods, such as sandblasting and wet-grinding [29,35]. For ZrO_2 , grinding has been recommended to create a surface region of compressive stresses, which increases the mean flexural strength of ZrO_2 . Noted that no surface treatment was used in the present study in order to keep the as-fabricated property, so the surface defects were unavoidable and resulted in the crack initiation points. It would be worthy of investigation the surface treatment on the fracture toughness of 3D printed ZrO_2 in the future.

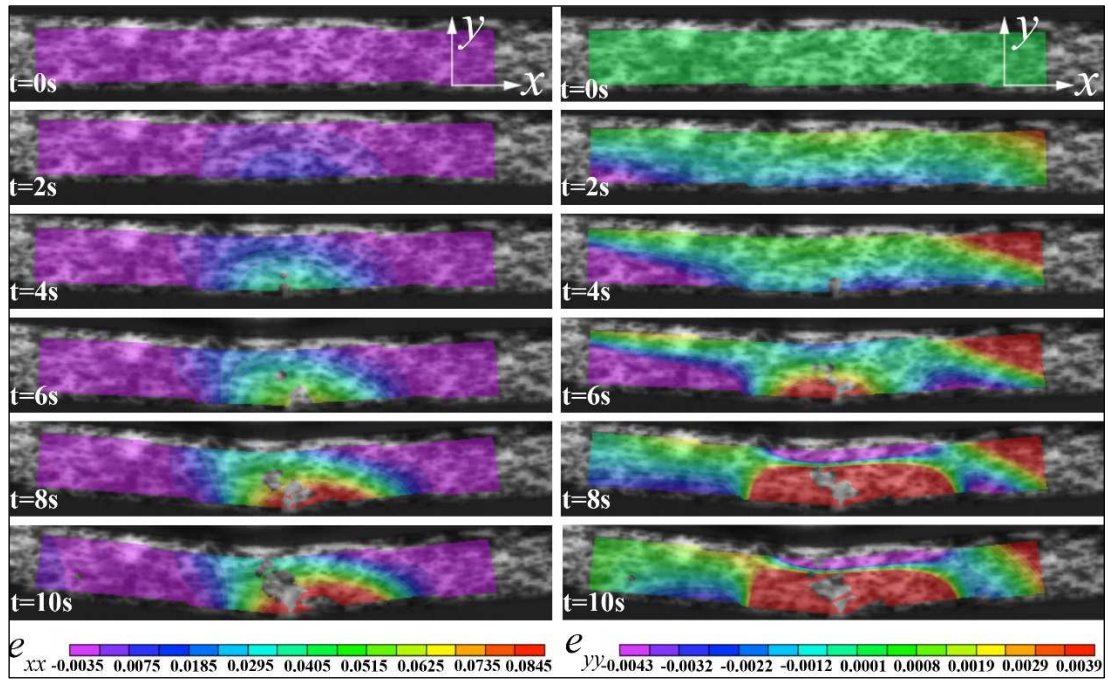


Fig. 8. The DIC images of the horizontal strain (e_{xx}) and the vertical strain (e_{yy}) of ZrO_2 samples under a three-point parallel bending test.

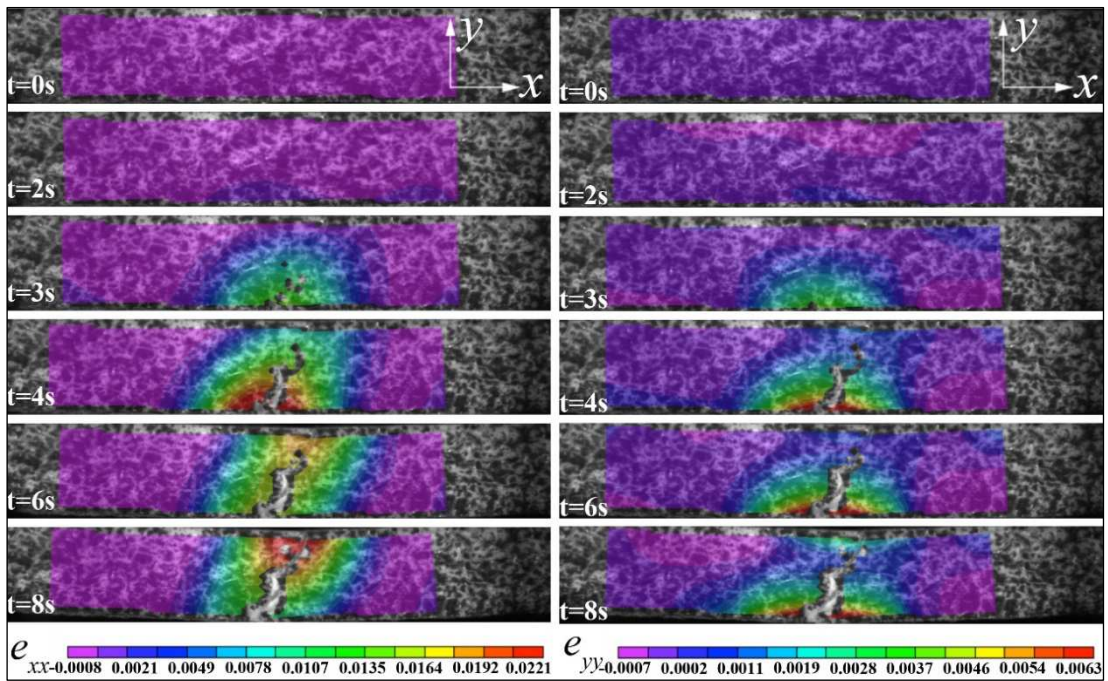


Fig. 9. The DIC images of the horizontal strain (e_{xx}) and the vertical strain (e_{yy}) of ZrO_2 samples under a three-point vertical bending test.

3.6. SEM

The SEM analysis can provide additional evidence for the microstructure of printed ZrO₂ samples (Fig. 10) and the fracture modes (Fig. 11-12).

Before sintering (green body), the top surface was flat and smooth without any visible cracks (Fig. 10a, 10b); however, after sintering, the top surface became coarse due to the shrinkage effect, and the cracks were observed (Fig. 10d, 10e). Moreover, the front surface exhibited a clear lamination along the printing direction (blue arrow) before and after sintering (Fig. 10c, 10f), which the interlayer was thinner after sintering.

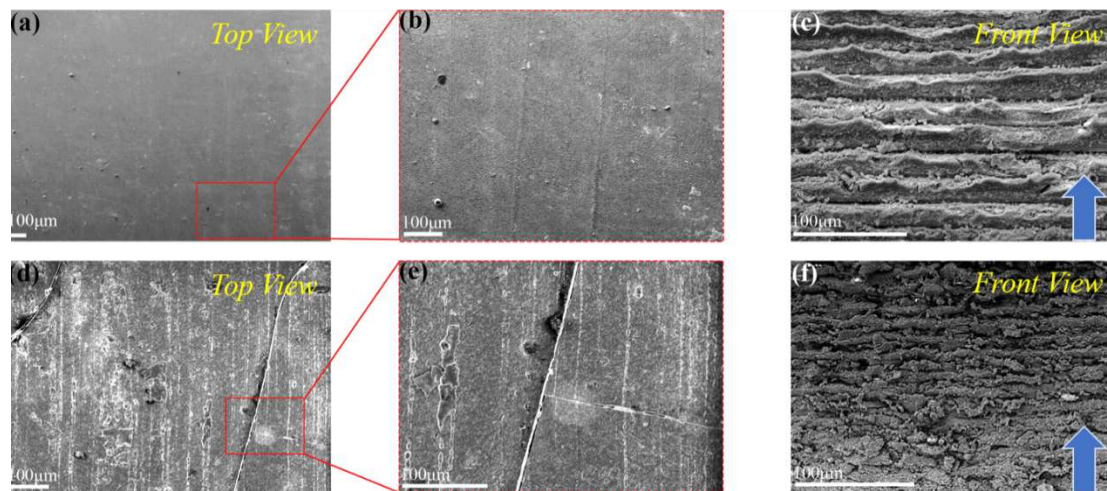


Fig. 10. The SEM images of 3D printing ZrO₂ specimen. (a-c): before sintering; (d-f): after sintering

The fracture morphology and its partially enlarged views for paralleling and vertical bending tests are displayed in Fig. 11 and 12, respectively. Although the samples appeared to be stacked layer by layer from the outside, they were actually interlaced with irregular and winding cracks, indicating the debinding and sintering process has a prominent influence on the interior microstructure.

The sintered ZrO₂ specimen was quite dense at depths of only a few hundred microns (as pointed with yellow rectangular in Fig. 11b and 12b), and this dense layer along the width direction was thicker than the printing direction. Moreover, the interior of the ZrO₂ specimen

was filled with needle-like cracks, meaning that the thermal diffusion in the debinding-sintering process and the mismatch of thermal expansion coefficient between resin (organic matter) and solid phase material determine the final microstructure. Meanwhile, such differences in internal and external microstructures also reflected that 3D printing technology might be more suitable for preparing spatial lattice structures with limited thickness to give full play of their strength rather than continuum bulk materials.

It can be seen that in the case of parallel loading, mainly the bottom printing layer was stretched to both lateral sides. Because the tensile strength of ceramic is typically much lower than the compressive strength, the failure started at the bottom first. However, under vertical loading, this bottom was a dense solidified layer, whose strength was significantly higher than that of the bottom layer with surface cracks under parallel loading, that's why the vertical bending strength was higher than that obtained in the parallel bending test.

In addition, the crack shape was different inside and outside. The dense outer layer was mainly composed of large and straight cracks between printing layers, whereas the interior contained numerous small winding cracks. When the big crack propagates and meets the small crack, the crack tip would be weakened, and the big crack may change propagation direction and decomposed into several small cracks (Fig. 13). As a result, the crack propagation would slow down, and some cracks may even be compressed and closed. Therefore, there was a large cleavage fracture morphology in the boundary layer (yellow rectangular in Fig. 11 and 12). Still, the plastic fracture mode (stepped morphology with blue ellipses) appeared in the interior (Fig. 12).

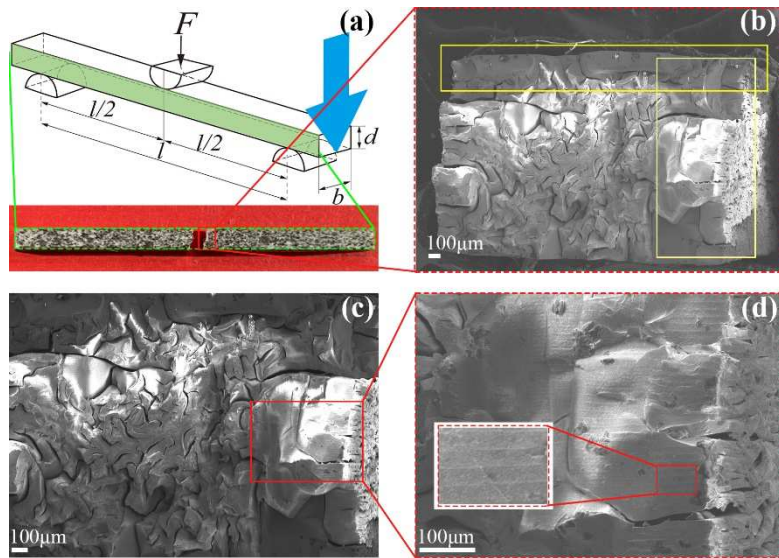


Fig. 11. The SEM images of three-point parallel loading. (a): Schematic diagram of the experiment; (b-d): Fracture morphology and its partial enlarged views.

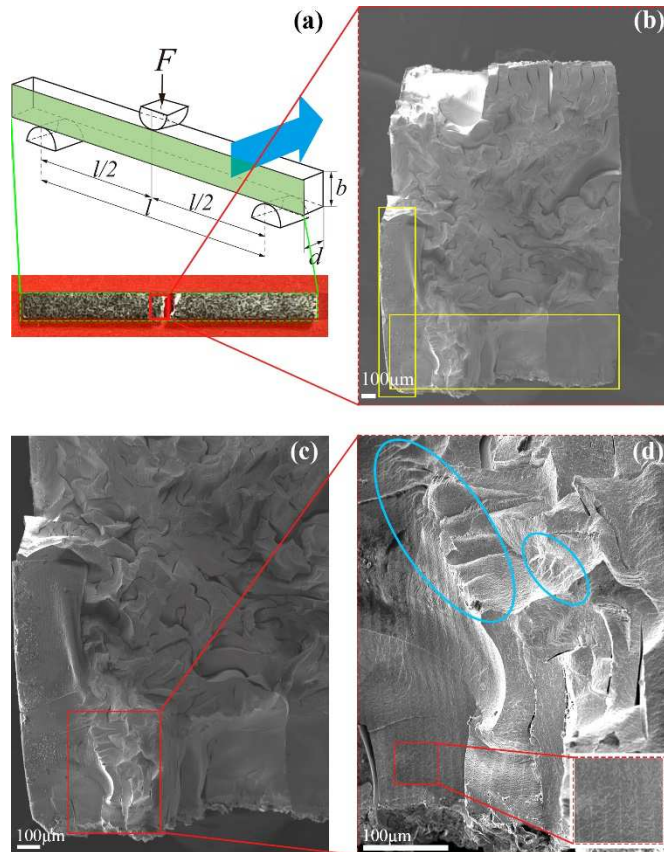


Fig. 12. The SEM images of three-point vertical loading. (a): Schematic diagram of the experiment; (b-d): Fracture morphology and its partial enlarged views.

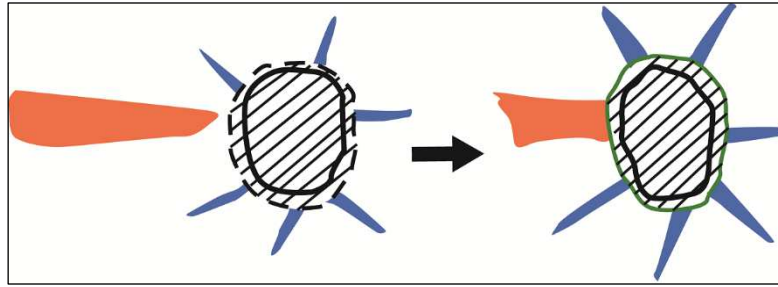


Fig. 13. The schematic diagrams of crack propagation.

Similar to other 3D printing technologies, there are still some challenges in the lamination process and sintering process of printing parts with DLP preparation technology [36]. It is expected that a more detailed study of the curing process itself is necessary for future development. For example, suppose the interaction between UV light and materials can be understood better. In that case, the DLP method can be comparable to other advanced ceramic processing techniques by fabricating structural products (i.e., bone scaffold).

4. Conclusion

ZrO₂ parts have been fabricated using a DLP 3D printing technology in which an attempt has been made to investigate its three-point bending deformation mechanism via DIC and fractography. The main conclusions are summarized as follows.

- The viscosity of the prepared slurry at 10 s⁻¹ and 100 s⁻¹ were 0.9 Pa·s and 0.13 Pa·s, respectively, which was desirable for processing.
- The relative density of the sintered ZrO₂ sample was approximately 98.8%, resulting in a Vickers hardness value of 1128 HV. The linear shrinkage was 41.74% on average.
- The crystalline phase of m-ZrO₂ and t-ZrO₂ were both detected in the original ZrO₂ powder; however, only the t-ZrO₂ phase remained in the sample after sintering up to 1500°C.
- The flexural strength under parallel and vertical bending loads were 56.63±3.97MPa and

70.98±6.62MPa, respectively. The crack propagates along the width direction (under vertical loading) was faster than that propagates along the thickness direction (under parallel loading).

- There was a large area of cleavage morphology in the dense boundary layers; still, the plastic fracture mode (stepped morphology with winding needle-like cracks) appeared in the interior of the sintered samples.

Declaration of competing interest

The authors declare that they have no known competing financial interests or personal relationships that could have influenced the work reported in this paper.

Acknowledgments

This work was financially supported by the Research Fund Program for Young Scholars of Beijing Institute of Technology. In addition, the authors would like to thank the engineers of Beijing 10 Dim tech. for their kind help with the DLP 3D printing process.

Reference

- [1] A. Arab, Z.D.I. Sktani, Q. Zhou, Z.A. Ahmad, P. Chen, Effect of MgO addition on the mechanical and dynamic properties of zirconia toughened alumina (ZTA) ceramics, *Materials (Basel)*. 12 (2019) 2440. <https://doi.org/10.3390/ma12152440>.
- [2] R. He, W. Liu, Z. Wu, D. An, M. Huang, H. Wu, Q. Jiang, X. Ji, S. Wu, Z. Xie, Fabrication of complex-shaped zirconia ceramic parts via a DLP- stereolithography-based 3D printing method, *Ceram. Int.* 44 (2018) 3412–3416. <https://doi.org/10.1016/j.ceramint.2017.11.135>.
- [3] A. Zocca, P. Colombo, C.M. Gomes, J. Günster, Additive Manufacturing of Ceramics: Issues, Potentialities, and Opportunities, *J. Am. Ceram. Soc.* 98 (2015) 1983–2001. <https://doi.org/10.1111/jace.13700>.

- [4] D.A. Komissarenko, P.S. Sokolov, A.D. Evstigneeva, I. V Slyusar, A.S. Nartov, P.A. Volkov, N. V Lyskov, P. V Evdokimov, V.I. Putlayev, A.E. Dosovitsky, DLP 3D printing of scandia-stabilized zirconia ceramics, *J. Eur. Ceram. Soc.* 41 (2021) 684–690. <https://doi.org/10.1016/j.jeurceramsoc.2020.09.010>.
- [5] N. Travitzky, A. Bonet, B. Dermeik, T. Fey, I. Filbert-Demut, L. Schlier, T. Schlordt, P. Greil, Additive manufacturing of ceramic-based materials, *Adv. Eng. Mater.* 16 (2014) 729–754. <https://doi.org/10.1002/adem.201400097>.
- [6] L.A. Nefedovaa, V.I. Ivkov, M.M. Sychov, S. V. Diachenko, M. V. Gravit, Additive manufacturing of ceramic insulators, in: *Mater. Today Proc.*, 2019: pp. 520–522. <https://doi.org/10.1016/j.matpr.2020.01.040>.
- [7] M.M. Methani, M. Revilla-León, A. Zandinejad, The potential of additive manufacturing technologies and their processing parameters for the fabrication of all-ceramic crowns: A review, *J. Esthet. Restor. Dent.* 32 (2020) 182–192. <https://doi.org/10.1111/jerd.12535>.
- [8] U. Scheithauer, E. Schwarzer, T. Moritz, A. Michaelis, Additive Manufacturing of Ceramic Heat Exchanger: Opportunities and Limits of the Lithography-Based Ceramic Manufacturing (LCM), *J. Mater. Eng. Perform.* 27 (2018) 14–20. <https://doi.org/10.1007/s11665-017-2843-z>.
- [9] E. Sachs, M. Cima, P. Williams, D. Brancazio, J. Cornie, Three dimensional printing: Rapid tooling and prototypes directly from a CAD model, *J. Manuf. Sci. Eng. Trans. ASME.* 114 (1992) 481–488. <https://doi.org/10.1115/1.2900701>.
- [10] S. Zakeri, M. Vippola, E. Levänen, A comprehensive review of the photopolymerization of ceramic resins used in stereolithography, *Addit. Manuf.* 35 (2020). <https://doi.org/10.1016/j.addma.2020.101177>.
- [11] H. Shao, D. Zhao, T. Lin, J. He, J. Wu, 3D gel-printing of zirconia ceramic parts, *Ceram. Int.* 43 (2017) 13938–13942. <https://doi.org/10.1016/j.ceramint.2017.07.124>.
- [12] M. Mohammadi, G. Becker, S. Diener, J.-M. Tulliani, N. Katsikis, P. Palmero, Robocasting of dense zirconia parts using commercial yttria-stabilized zirconia granules and ultrafine particles. Paste preparation, printing, mechanical properties, *Ceram. Int.* (2021). <https://doi.org/10.1016/j.ceramint.2021.09.278>.
- [13] S. Venkatesh, S.H. Rahul, K. Balasubramanian, Inkjet printing yttria stabilized zirconia coatings on porous and nonporous substrates, *Ceram. Int.* 46 (2020) 3994–3999. <https://doi.org/10.1016/j.ceramint.2019.09.298>.

- [14] T. Shen, H. Xiong, Z. Li, L. Zhang, K. Zhou, Fused deposition fabrication of high-quality zirconia ceramics using granular feedstock, *Ceram. Int.* (2021). <https://doi.org/10.1016/j.ceramint.2021.08.348>.
- [15] H. Zhang, C. Jiao, Z. He, M. Ge, Z. Tian, C. Wang, Z. Wei, L. Shen, H. Liang, Fabrication and properties of 3D printed zirconia scaffold coated with calcium silicate/hydroxyapatite, *Ceram. Int.* 47 (2021) 27032–27041. <https://doi.org/10.1016/j.ceramint.2021.06.116>.
- [16] M. Shen, W. Zhao, B. Xing, Y. Sing, S. Gao, C. Wang, Z. Zhao, Effects of exposure time and printing angle on the curing characteristics and flexural strength of ceramic samples fabricated via digital light processing, *Ceram. Int.* 46 (2020) 24379–24384. <https://doi.org/10.1016/j.ceramint.2020.06.220>.
- [17] J. Lu, P. Dong, Y. Zhao, Y. Zhao, Y. Zeng, 3D printing of TPMS structural ZnO ceramics with good mechanical properties, *Ceram. Int.* 47 (2021) 12897–12905. <https://doi.org/10.1016/j.ceramint.2021.01.152>.
- [18] C.Y. Su, J.C. Wang, D.S. Chen, C.C. Chuang, C.K. Lin, Additive manufacturing of dental prosthesis using pristine and recycled zirconia solvent-based slurry stereolithography, *Ceram. Int.* 46 (2020) 28701–28709. <https://doi.org/10.1016/j.ceramint.2020.08.030>.
- [19] K.J. Jang, J.H. Kang, J.G. Fisher, S.W. Park, Effect of the volume fraction of zirconia suspensions on the microstructure and physical properties of products produced by additive manufacturing, *Dent. Mater.* 35 (2019) e97–e106. <https://doi.org/10.1016/j.dental.2019.02.001>.
- [20] C. Feng, K. Zhang, R. He, G. Ding, M. Xia, X. Jin, C. Xie, Additive manufacturing of hydroxyapatite bioceramic scaffolds: Dispersion, digital light processing, sintering, mechanical properties, and biocompatibility, *J. Adv. Ceram.* 9 (2020) 360–373. <https://doi.org/10.1007/s40145-020-0375-8>.
- [21] F. Lu, R. Wu, M. Shen, L. Xie, M. Liu, Y. Li, S. Xu, L. Wan, X. Yang, C. Gao, Z. Gou, Rational design of bioceramic scaffolds with tuning pore geometry by stereolithography: Microstructure evaluation and mechanical evolution, *J. Eur. Ceram. Soc.* 41 (2021) 1672–1682. <https://doi.org/10.1016/j.jeurceramsoc.2020.10.002>.
- [22] J. Sun, J. Binner, J. Bai, 3D printing of zirconia via digital light processing: optimization of slurry and debinding process, *J. Eur. Ceram. Soc.* 40 (2020) 5837–5844. <https://doi.org/10.1016/j.jeurceramsoc.2020.05.079>.
- [23] M. Zhang, R. Lin, X. Wang, J. Xue, C. Deng, C. Feng, H. Zhuang, J. Ma, C. Qin, L. Wan, J. Chang, C. Wu, 3D printing of Haversian bone-mimicking scaffolds for multicellular delivery in bone regeneration, *Sci. Adv.* 6 (2020). <https://doi.org/10.1126/sciadv.aaz6725>.

- [24] A. Della Bona, O.E. Pecho, R. Alessandretti, Zirconia as a dental biomaterial, *Materials (Basel)*. 8 (2015) 4978–4991. <https://doi.org/10.3390/ma8084978>.
- [25] X. Xia, G. Duan, Effect of solid loading on properties of zirconia ceramic by direct ink writing, *Mater. Res. Express*. 8 (2021). <https://doi.org/10.1088/2053-1591/abd866>.
- [26] T. Yu, Z. Zhang, Q. Liu, R. Kuliiev, N. Orlovskaya, D. Wu, Extrusion-based additive manufacturing of yttria-partially-stabilized zirconia ceramics, *Ceram. Int.* 46 (2020) 5020–5027. <https://doi.org/10.1016/j.ceramint.2019.10.245>.
- [27] J. Sun, J. Binner, J. Bai, 3D printing of zirconia via digital light processing: optimization of slurry and debinding process, *J. Eur. Ceram. Soc.* 40 (2020) 5837–5844. <https://doi.org/10.1016/j.jeurceramsoc.2020.05.079>.
- [28] C.J. Bae, A. Ramachandran, K. Chung, S. Park, Ceramic stereolithography: Additive manufacturing for 3D complex ceramic structures, *J. Korean Ceram. Soc.* 54 (2017) 470–477. <https://doi.org/10.4191/kcers.2017.54.6.12>.
- [29] J. Sun, J. Binner, J. Bai, Effect of surface treatment on the dispersion of nano zirconia particles in non-aqueous suspensions for stereolithography, *J. Eur. Ceram. Soc.* 39 (2019) 1660–1667. <https://doi.org/10.1016/j.jeurceramsoc.2018.10.024>.
- [30] K. Wang, M. Qiu, C. Jiao, J. Gu, D. Xie, C. Wang, X. Tang, Z. Wei, L. Shen, Study on defect-free debinding green body of ceramic formed by DLP technology, *Ceram. Int.* 46 (2020) 2438–2446. <https://doi.org/10.1016/j.ceramint.2019.09.237>.
- [31] Z. Mei, Y. Lu, Y. Lou, P. Yu, M. Sun, X. Tan, J. Zhang, L. Yue, H. Yu, Determination of Hardness and Fracture Toughness of Y-TZP Manufactured by Digital Light Processing through the Indentation Technique, *Biomed Res. Int.* 2021 (2021). <https://doi.org/10.1155/2021/6612840>.
- [32] M.R. Gauna, M.S. Conconi, S. Gomez, G. Suárez, E.F. Aglietti, N.M. Rendtorff, Monoclinic-tetragonal zirconia quantification of commercial nanopowder mixtures by XRD and DTA, *Ceram. - Silikaty*. 50 (2015) 318–325.
- [33] A.K.S. S. N. Khan, R. M. Warkhedkar, Human bone strength evaluation through different mechanical tests, *Int. J. Curr. Eng. Technol.* (2014) 539–543.
- [34] M. Borba, M.D. De Araújo, E. De Lima, H.N. Yoshimura, P.F. Cesar, J.A. Griggs, Á. Della Bona, Flexural strength and failure modes of layered ceramic structures, *Dent. Mater.* 27 (2011) 1259–1266. <https://doi.org/10.1016/j.dental.2011.09.008>.

[35] M. Guazzato, L. Quach, M. Albakry, M. V. Swain, Influence of surface and heat treatments on the flexural strength of Y-TZP dental ceramic, *J. Dent.* 33 (2005) 9–18. <https://doi.org/10.1016/j.jdent.2004.07.001>.

[36] W. Oropallo, L.A. Piegler, Ten challenges in 3D printing, *Eng. Comput.* 32 (2016) 135–148. <https://doi.org/10.1007/s00366-015-0407-0>.